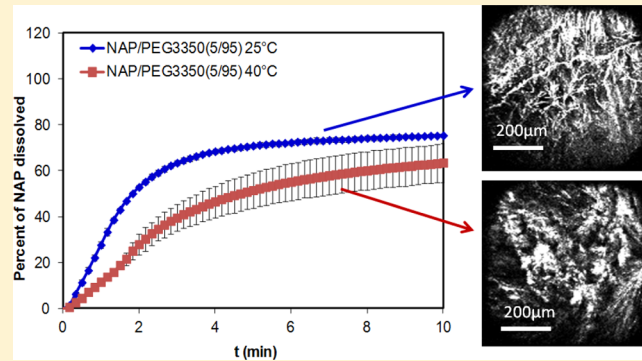


Crystallization and Dissolution Behavior of Naproxen/Polyethylene Glycol Solid Dispersions

Qing Zhu,[†] Scott J. Toth,[‡] Garth J. Simpson,[‡] Hsin-Yun Hsu,[†] Lynne S. Taylor,^{*,§} and Michael T. Harris^{*,†}

[†]School of Chemical Engineering, [‡]Department of Chemistry, and [§]Department of Industrial and Physical Pharmacy, Purdue University, West Lafayette, Indiana 47907, United States

ABSTRACT: The crystallization kinetics of naproxen (NAP) in NAP/polyethylene glycol (NAP/PEG) solid dispersions prepared at different crystallization temperatures was studied by *in situ* small-angle X-ray scattering/wide-angle X-ray scattering (SAXS/WAXS). It was found that the crystallization rate of NAP was faster at 25 °C in comparison to 40 °C. This resulted in different sizes of NAP domains, and consequently impacted the dissolution behavior. The sizes of NAP domains prepared at 40 °C were larger than those at 25 °C, as determined with surface area analysis, utilizing second-order nonlinear optical imaging of chiral crystals (SONICC). Consistent with this observation, the corresponding dissolution rate of the NAP/PEG dispersion prepared at 40 °C was indeed slower than that prepared at 25 °C. The microstructure of the NAP/PEG solid dispersions and the dissolution behavior also showed a dependence on the chemical composition of the solid dispersions.



1. INTRODUCTION

The formulation of poorly water-soluble active pharmaceutical ingredients (API) has become a major challenge in drug development as the number of water-insoluble APIs has increased.¹ Solid dispersion of an API within a polymeric carrier can enhance the bioavailability of many APIs with low aqueous solubility.^{1–4} Most solid dispersions are prepared using highly water-soluble polymers as the carrier, where the polymer can be amorphous (e.g., polyvinylpyrrolidone (PVP)) or partially crystalline (e.g., polyethylene glycol (PEG)). Amorphous polymers are typically used to inhibit the crystallization of APIs and produce molecular dispersed amorphous dispersions^{1,3} or amorphous drug nanoparticles stabilized by polymers.^{5,6} For dispersions prepared with a semicrystalline polymeric carrier, the phase behavior of the system can be very complex.^{2–4,7–13} Polyethylene glycol (PEG), a semicrystalline and hydrophilic polymer, has been widely used as a polymeric carrier to enhance the delivery of various APIs.^{1,2,7,8} In previous studies, it has been found that PEG can delay, promote, or have no significant influence on the crystallization kinetics of different APIs.¹⁴ It also has been observed that the microstructure of API–PEG systems is complex and can change with time.^{15,16}

It is still unclear how the crystallization conditions and API–polymer interactions influence the final size and spatial distribution of the API in the polymer matrix. It is anticipated that the microstructure will affect the dissolution behavior; although to date, no clear correlation has been made between the structure of the API/PEG dispersions and the correspond-

ing dissolution performance. This is undoubtedly due, in large part, to the difficulties associated with probing the location and distribution of the API within a polymer matrix.

In this study, naproxen ((+)-(S)-2-(6-methoxynaphthalen-2-yl) propanoic acid, NAP) was chosen as the model API to form a solid dispersion with PEG. NAP is chiral, and the S enantiomer is used therapeutically. Because it is chiral and hence crystallizes in a chiral space group (P_{2_1}), it is likely to show the effect of second harmonic generation (SHG), or frequency doubling of light when in crystalline form. Consequently, NAP can be potentially selectively detected and imaged in a NAP/PEG solid dispersion by the recently developed second-order nonlinear optical imaging of chiral crystals (SONICC) technique.^{17–19} The goal of this study was to evaluate the crystallization kinetics of NAP/PEG solid dispersions and to correlate the crystallization behavior with the resultant API microstructure in the polymer matrix and the dissolution rate of the API.

2. MATERIALS AND METHODS

Materials and Sample Preparation. Naproxen (NAP) was purchased from Spectrum Chemical (Gardena, CA). PEG with a molecular weight 3350 was a kind gift from The Dow Chemical Co. (Midland, MI). The structures of NAP and PEG are shown in Figure 1. Physical mixtures of the API and PEG

Received: October 28, 2012

Revised: December 4, 2012

Published: January 15, 2013

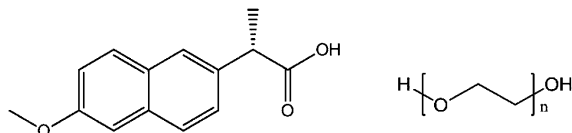


Figure 1. Structure of NAP (left) and PEG (right).

were prepared by simple geometric mixing of the two pure components (a total of 1 g of powder) for 20 min using a spatula, and dispersions were made by melting the mixtures for enough time to ensure complete melting and allowing them to solidify at either 25 or 40 °C. Following solidification, the samples were stored in desiccators at low relative humidity. These crystallization temperatures were chosen to represent room temperature storage and at temperature intermediate to room temperature and the melting temperature of PEG.

Time-Resolved Simultaneous Small-Angle X-ray Scattering/Wide-Angle X-ray Scattering (SAXS/WAXS). The simultaneous SAXS/WAXS experiments were conducted at the Advanced Photon Source beam station 12-ID-B, Argonne National Laboratory. The small-angle X-ray scattering instrument was equipped with a Pilatus 2 M detector, and the wide-angle X-ray scattering system was equipped with a Pilatus 300K detector. The energy of the X-ray source was 12 keV ($\lambda = 1.0 \text{ \AA}$), and the distance of the sample to the SAXS and WAXS detectors was 2010 and 491 mm, respectively. The q (scattering vector) range was $0.0053\text{--}2.12 \text{ \AA}^{-1}$. The SAXS/WAXS range was calibrated using silver behenate (AgBeh), and the absolute intensity was calibrated using glassy carbon. Physical mixtures of NAP and PEG by geometrical mixing (prepared as described above) were added to small aluminum pans (Tzero DSC sample pans, TA Instruments, New Castle, DE) and subjected to a temperature cycle using a Linkam THMS600 stage controlled by a Linkam CI 93 temperature programmer (Linkam Scientific Instruments Ltd., Surrey, UK). The sample was first heated to above the melting point of NAP, followed by quench cooling to the specific solidification temperatures. The time required for complete melting of the sample was determined by monitoring the WAXS pattern to ensure that all of the diffraction peaks had disappeared.

Second-Order Nonlinear Optical Imaging of Chiral Crystals (SONICC). A SONICC instrument was utilized to image NAP/PEG dispersions. A 50 mW, 800 nm incident beam of the SONICC instrument was generated by a Spectra-Physics Mai Tai HP Ti:Sapphire laser, with a pulse repetition rate of 80 MHz, and pulse width of ~150 fs. The focal volume was scanned across the sample with both a galvanometer (slow-axis) and vibrating mirror (~4 kHz, fast-axis), minimizing thermal sample perturbations. The beam was directed onto the NAP/PEG solid dispersions with a 10× objective (Nikon, 0.3 NA). The sample was placed onto an automated Prior Scientific OptiScan XYZ stage, with the temperature maintained by a Linkam THMS 600 hot-stage, and Linkam temperature controller. The resultant SHG signal reflected off 400 nm dichroic mirrors, selectively directing the frequency-doubled light into the epi and transmission photomultiplier tubes (PMTs) (Burle VD189). The current transient signals from the PMTs were amplified with Ortec 9305 amplifiers, and then directed into Becker and Hickl GmbH PMS-400A photon-counting cards, utilizing Labview software designed by the Jonathan Amy Facility for Chemical Instrumentation at Purdue University and Mike Everly. The acquired images were then

subsequently analyzed using ImageJ software developed by NIH, in addition to Matlab.

Fourier Transform Infrared Spectroscopy (FTIR). The infrared spectra for the pure materials and NAP/PEG (20/80% w/w) mixtures in the molten state were collected using a Bio-Rad FTS-6000 (Bio-Rad, Cambridge, MA) equipped with an attenuated total reflectance accessory (diamond crystal, Golden Gate, Graseby Specac, Inc., Cranston, RI). The sample (~20 mg) was scanned between 500 and 4000 cm⁻¹ wavenumber, resolution of 4 cm⁻¹, and 128 scans. The system was purged with dry, CO₂-free air.

Hot-Stage Microscopy. The API and PEG were physically mixed as described above, heated to the melting point of the API to form a homogeneous melt, and followed by cooling to allow solidification. After storage for a few days (actual time depended on the crystallization rate of the API) at low relative humidity, the API/PEG solid dispersions were ground using a mortar and pestle. The resultant powder was evaluated using a Nikon Eclipse E600 polarized light microscope (Nikon Inc., Melville, NY) equipped with a Linkam THMS 600 hot-stage (Linkam Scientific Instruments Ltd., Surrey, UK). The samples were heated at 1 °C/min until completely melted. The temperature where the last crystal melted was recorded and was used to construct the phase diagram.

Dissolution Testing Using Ultraviolet–Visible (UV–Vis) Spectroscopy. A physical mixture of the API and PEG was placed in an aluminum cell with a constant surface area ($d = 1 \text{ cm}$), heated until completely melted, followed by solidification using a kapton film on top to yield a smooth, flat surface with constant surface area (in the form of a slab). After solidification, the kapton film was removed, and the sample in the aluminum cell was subjected to dissolution testing using a buffer solution (900 mL) at pH 2 at 37 °C. Sink conditions and constant pH were assumed. A model 400 UV-vis spectrometer equipped with a fiber optic dip probe (having a 5 mm optical path length) (SI photonics Inc., Tucson, AZ) was employed to collect the spectra at constant time intervals. The absorbance at a wavelength of 249 nm was used to calculate the concentration of NAP, using the Beer–Lambert relationship. NAP solutions with concentration of 0, 0.0002, 0.005, 0.001, 0.002, and 0.004 mg/mL were used to construct the standard curve, and the calculated R^2 for the standard curve was 1, indicating a good linear relationship between the concentration of NAP and the UV absorbance.

3. RESULTS AND DISCUSSION

Phase Behavior of NAP/PEG Systems. The phase diagram for NAP/PEG (Figure 2) was constructed using optical microscopy to determine the melting point depression of mixtures of various compositions. It shows that NAP/PEG is a eutectic system with a eutectic composition of 15% NAP. The interaction parameter, χ , between NAP and PEG was determined to be -0.28, using the methods described previously.^{15,16,20–23} The negative interaction parameter suggests the formation of specific favorable interactions between molten NAP and PEG, which were demonstrated using FTIR spectroscopy as shown in Figure 3. Figure 3 shows a comparison between the spectrum of a physical mixture (constructed from the pure spectra as described by Rumondor et al.²⁴) and the experimental spectrum of a NAP–PEG mixture in the molten state. If no NAP–PEG interactions are present, the physical mixture spectrum should be very similar to the experimental spectrum. However, the shift of the peak

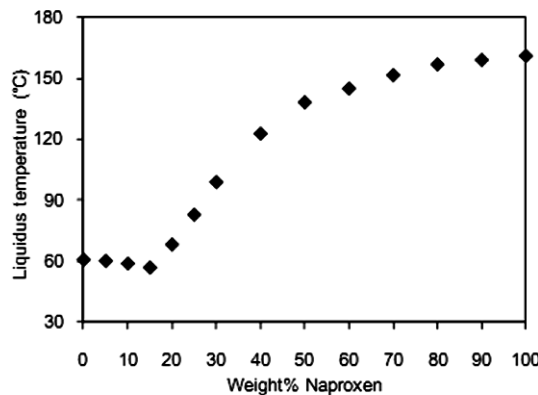


Figure 2. Phase diagram of NAP/PEG3350.

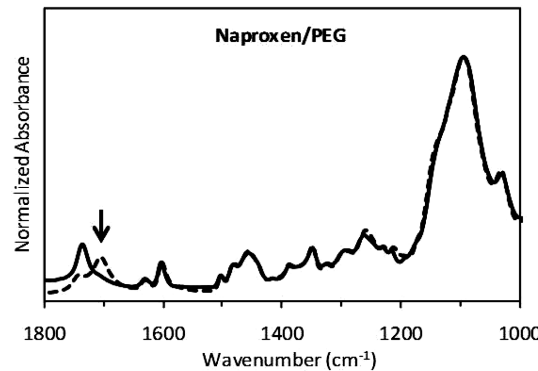


Figure 3. FTIR spectra of NAP/PEG3350 (20/80) (w/w) mixture at molten state: Solid (—) and dashed (---) lines represent the experimentally measured and calculated physical mixture spectra, respectively. The arrow shows the change in the NAP carboxylic acid carbonyl peak in the presence of PEG, indicating the formation of API-PEG hydrogen bonds.

position at around 1700 cm^{-1} (carbonyl region, peak arises from NAP carboxylic acid function) between the experimental and calculated spectrum of NAP-PEG mixture indicated the formation of hydrogen bonds between NAP and PEG.^{15,16}

Crystallization Kinetics and Structural Evolution of NAP/PEG Solid Dispersions. The crystallization kinetics of NAP and the structural evolution of PEG lamellae in the NAP/PEG solid dispersions were studied simultaneously using time-resolved SAXS/WAXS. WAXS was used to study the crystallization kinetics of NAP, while SAXS was used to understand how the PEG lamellae evolved with time. Figure 4 shows the SAXS/WAXS profiles of NAP/PEG system at different time points during solidification at $25\text{ }^{\circ}\text{C}$. The horizontal axis is the scattering vector q , a length scale in reciprocal space. During solidification of NAP/PEG (20/80) systems at $25\text{ }^{\circ}\text{C}$, at $t = 0\text{ min}$, there were no diffraction peaks in SAXS/WAXS profile, consistent with a supercooled melt. As time increased to $t = 0.1\text{ min}$, a small peak appeared at $q = 0.037\text{ \AA}^{-1}$ in the SAXS region, and another two peaks presented at $q = 1.36$ and 1.66 \AA^{-1} in the WAXS profile. The diffraction peak at $q = 0.037\text{ \AA}^{-1}$ in the SAXS region was due to the orderly packing of PEG lamellae, while the two peaks at 1.36 and 1.66 \AA^{-1} in the WAXS profile were characteristic peaks of crystalline PEG.^{16,25,26} Shortly thereafter, the intensity of the diffraction peak arising from crystalline PEG increased to a maximum value, indicating that PEG crystallized virtually immediately after solidification. At around $t = 6.7\text{ min}$, several

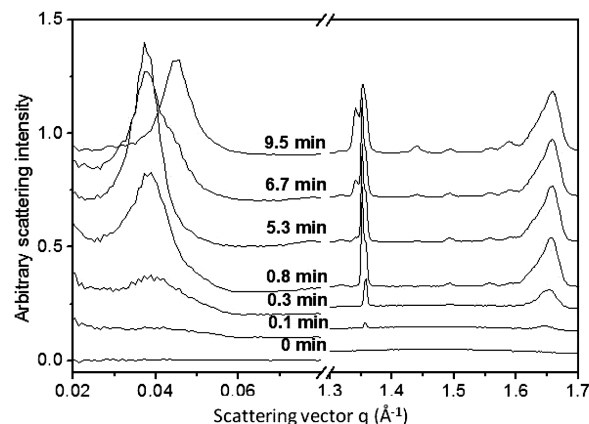


Figure 4. SAXS/WAXS data of NAP/PEG3350 (2/8) at $25\text{ }^{\circ}\text{C}$.

new diffraction peaks at $q = 1.32$ and 1.44 \AA^{-1} appeared, due to the crystallization of NAP. Over the next few minutes, the intensity of those peaks increased, while concurrently, the diffraction peak at around $q = 0.037\text{ \AA}^{-1}$ (due to the PEG lamellae) shifted to $q = 0.046\text{ \AA}^{-1}$. The long period (L) of PEG lamellar structure can be calculated from Bragg's Law, that is, $L = 2n\pi/q$, in which q is the scattering vector of the diffraction peak, n is the order of diffraction ($n = 1$), and π is a constant. On the basis of Bragg's law, the long period (L) decreased from 17.0 to 13.7 nm within a few minutes. The large decrease of the long period indicated that most of the amorphous NAP crystallized over this time frame, and consequently was no longer associated with the interlamellar region of PEG matrix, as observed previously for other API-PEG systems.¹⁶ When the NAP/PEG system was solidified at $40\text{ }^{\circ}\text{C}$, similar events were observed (Figure 5). PEG crystallized first, followed by

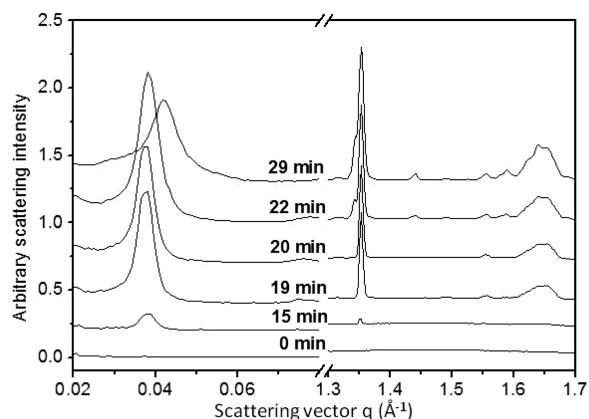


Figure 5. SAXS/WAXS data of NAP/PEG3350 (2/8) at $40\text{ }^{\circ}\text{C}$.

NAP crystallization, whereby the crystallization of NAP resulted in a large shift of the diffraction peak (around 0.037 \AA^{-1}) in the SAXS region.

To study the crystallization kinetics of NAP in the dispersions, the percentage of crystalline NAP at time t , denoted as $X(t)$, was calculated by integrating the area under the NAP diffraction peaks ($q = 1.32$ and 1.44 \AA^{-1}) at time t ($\Phi_{\text{NAP}}(t)$), and normalized by the area under the NAP diffraction peaks when crystallization was complete ($\Phi_{\text{NAP}}(\infty)$).^{27,28}

$$X(t) = \Phi_{\text{NAP}}(t)/\Phi_{\text{NAP}}(\infty) \quad (1)$$

Figure 6 shows the crystallization kinetics of NAP in the NAP/PEG solid dispersions crystallized at 25 and 40 °C. The

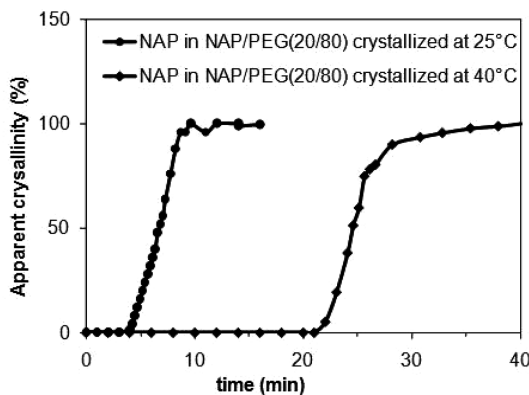


Figure 6. Crystallization kinetics of NAP in NAP/PEG3350 (20/80) at 25 and 40 °C by SAXS/WAXS.

induction time for crystallization of NAP at 25 °C (5 min) was much shorter than that at 40 °C (20 min). Figure 6 also shows that the overall crystallization kinetics at 25 °C was faster than that at 40 °C. However, when NAP crystallized in the absence of PEG, it started to crystallize during the cooling process before even reaching 40 °C, taking only a few seconds to crystallize completely.

Structure and Spatial Distribution of NAP in the Solid Dispersions. It is important to know the size range of the NAP and the distribution of API in the polymer matrix, to fully understand the link between dispersion microstructure and

dissolution performance. NAP crystallizes in a chiral space group and can consequently be selectively detected using the SONICC technique. SONICC is based on second harmonic generation (SHG), a nonlinear optical effect, exhibited by chiral, noncentrosymmetric crystalline materials.^{17–19} The NAP crystals give substantial signal, corresponding to the white areas in the SHG images (Figure 7), while the lack of signal from the PEG matrix yields black areas using this imaging technique, because PEG is present either in an amorphous state or in a centrosymmetric microcrystalline form (the majority of achiral molecules adopt centrosymmetric SHG-inactive lattices upon crystallization). Figure 7 shows the spatial distribution of crystalline NAP in the PEG matrix prepared at different crystallization temperatures and compositions, as well as the edges of crystalline domains. The images in Figure 7g–i are representative edge detection images for the SHG images in Figure 7d–f, the 40 °C samples, and were generated with the Canny edge detection algorithm in Matlab. This allows for the quantification of differences in surface area from one sample to the next. The algorithm has inputs for low and high thresholds, allowing edges to be found even for overlapping crystalline domains, as long as there are intensity differences. The acquired SHG images were imported to Matlab, and black and white images were generated, with pixels on crystal edges assigned the value of 1, and all other nonedge pixels were given the value of 0. Averaging the pixel intensities over each field of view results in fractional values ψ , where a larger value indicates the presence of more surface area than a smaller number (i.e., larger edge fraction corresponds to smaller crystalline domains, with surface area scaling quadratically with ψ). If the dissolution rate is dictated primarily by surface area of the crystallites, the

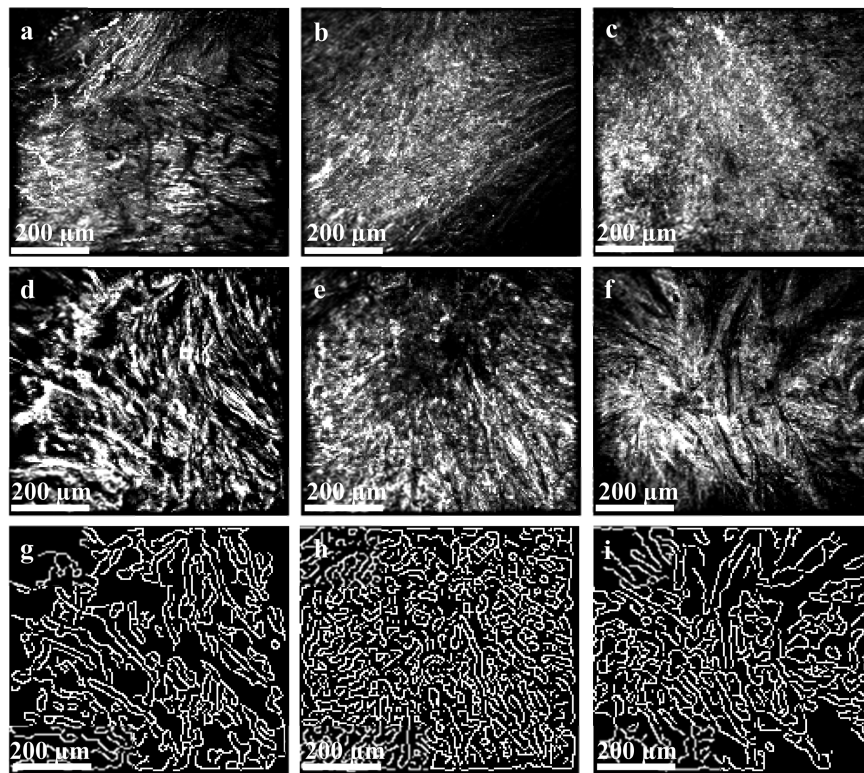


Figure 7. SHG images of NAP/PEG solidified for 24 h with composition: (a) 25 °C, 5/95 (% w/w); (b) 25 °C, 10/90; (c) 25 °C, 20/80; (d) 40 °C, 5/95; (e) 40 °C, 10/90; (f) 40 °C, 20/80; (g) edge detection of 40 °C, 5/95; (h) edge detection of 40 °C, 10/90; (i) edge detection of 40 °C, 20/80.

differences in rates should correlate loosely with the differences in ψ^2 values. The crystallization of NAP at 40 °C results in the formation of larger crystal domains than at 25 °C, in particular for the solid dispersions containing 5% or 10% NAP. The sample with 5% NAP at 25 °C resulted in an edge fraction of 0.26, whereas the 5% NAP at 40 °C resulted in an edge fraction of 0.20, confirming larger crystalline domains for the sample with the higher crystallization temperature. When the weight percent of the NAP was increased to 20%, the NAP domains were still larger at 40 °C, although the differences were not as obvious due to the substantial increase in crystalline content, and edge detection methods were not as effective.

In addition to the effect of the crystallization temperature on the structure of NAP, the spatial distribution of the NAP also varied dramatically when the weight percent of the NAP was changed in the solid dispersions. For the NAP/PEG (5/95) solid dispersion crystallized at 25 °C, the distribution of the NAP was not uniform across the matrix, and distinct "black" regions can be observed, due to the PEG matrix. The crystals appear to form branched-like structures where the branches are a few micrometers in length. When the content of NAP was increased to 10% or above, the distribution of crystalline material becomes more uniform across the matrix. The increase in density of the crystalline material is clearly visible as the weight percent of NAP increases.

Dissolution Behavior of NAP/PEG3350 Solid Dispersions. From the above study, it is found that the size and spatial distribution of NAP in the dispersions varied when the crystallization temperature and composition of the system were different. It is considered likely that these differences in microstructure influence the dissolution behavior. To test this hypothesis, dissolution profiles of NAP/PEG (5/95) dispersions crystallized at both 25 and 40 °C were recorded, shown in Figure 8. It was observed that the initial dissolution

surface areas for the sample prepared at 25 °C to that at 40 °C is approximately 1.7. This also indicates that the dissolution rate of NAP was dictated by surface areas for the sample with 5% NAP in PEG matrix. For a constant mass of NAP, smaller API domains will result in an increase in the surface area in contact with the aqueous dissolution medium. The dissolution kinetics of NAP/PEG solid dispersions with different NAP weight percents was also investigated (Figure 9). Figure 9 shows that

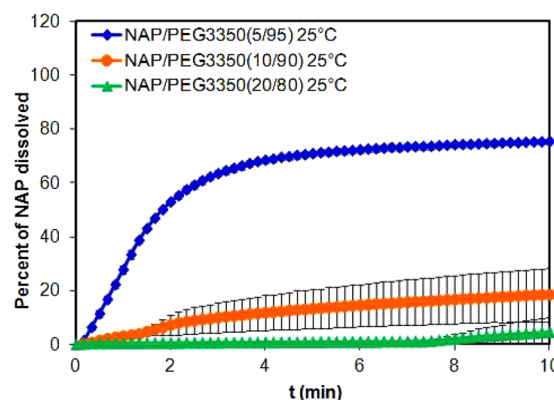


Figure 9. Dissolution profiles of NAP/PEG3350 with different compositions crystallized at 25 °C.

the dissolution rate of NAP/PEG (5/95) was the fastest, while the solid dispersion containing 20% NAP dissolved considerably more slowly, with little drug released over the time period monitored.

In previous studies, it was observed that API–PEG interactions may slow the crystallization of the API in the dispersions,¹⁴ which appears to also be true for the NAP/PEG systems, because NAP crystallization in the dispersions is delayed relative to pure NAP. The crystallization behavior of NAP in the solid dispersions shows variance when prepared at different crystallization temperatures. The overall crystallization rate of NAP at 25 °C is faster than that at 40 °C, which will result in different sizes of NAP domains in PEG matrix. When the NAP/PEG system is crystallized at 25 °C, the nucleation rate is expected to be higher than at 40 °C due to the higher extent of supercooling and hence larger thermodynamic driving force for crystallization. Nucleation kinetics is anticipated to be controlled by thermodynamic factors in undercooled melts close to the melting point,²⁹ as for this system, see phase diagram in Figure 2. If this is indeed the case, NAP domains will be formed with an increased frequency and smaller size. This prediction is consistent with the SHG images of the NAP/PEG solid dispersions; the NAP/PEG sample prepared at 40 °C formed larger NAP domains than that at 25 °C for the same composition. Interestingly, there is a remarkable difference in terms of the spatial distribution of the NAP in PEG matrix when the chemical composition is varied. This difference in structure has a substantial impact on dissolution behavior, where the lower concentration API dispersion exhibits faster dissolution kinetics than for samples where the API concentration is increased from 5% to 10% to 20% w/w. The higher dissolution rate of NAP in the 5% dispersions may be due to the reduced number of NAP–NAP crystal contact points in the dispersion, resulting in more isolated regions of NAP that can have more interaction with the solvent upon PEG dissolution, relative to the higher API concentration dispersions, where the NAP crystals appear to form a fairly

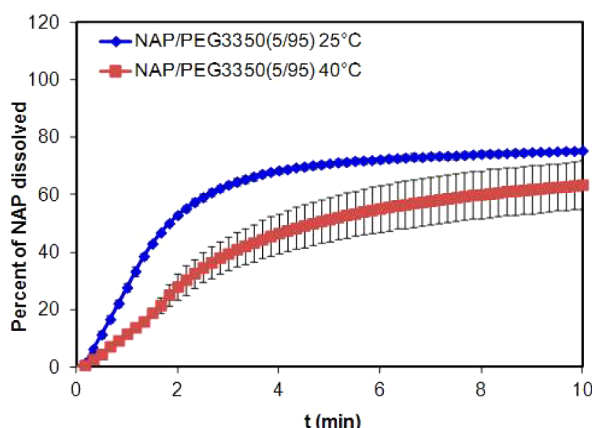


Figure 8. Dissolution behavior of NAP/PEG3350 (5/95) crystallized at both 25 and 40 °C (the error bar for the dissolution profile of NAP/PEG (5/95) prepared at 25 °C is smaller than the symbol size).

rate of the NAP/PEG system prepared at 25 °C was faster than that of the NAP/PEG system prepared at 40 °C, approximately twice as fast as the dissolution rate for the sample prepared at 40 °C. The faster dissolution rate when the NAP/PEG sample was prepared at 25 °C is attributed to the smaller NAP domain size, corresponding strongly with the previously mentioned edge detection surface area estimates. The ratio of the square of the fraction values ψ^2 for the sample prepared at 25 °C to that at 40 °C with 5% NAP is around 1.7, indicating that the ratio of

continuous network. SONICC appears to be an informative imaging technique to evaluate the spatial distribution of chiral crystals in a polymeric matrix.

4. CONCLUSION

Crystallization kinetics of NAP in NAP/PEG dispersions were reduced as compared to that of pure NAP and were also dependent on the crystallization temperature. The faster overall crystallization rate when solidified at 25 °C as compared to that at 40 °C resulted in smaller NAP domains in the matrix, as confirmed by quantifying the amount of crystal surface area in SHG images with an edge detection algorithm. The SONICC technique has been applied for the first time to image the distribution of chiral API crystals in a polymer matrix and is a potentially important tool to understand correlations between the structure of a solid dispersion and important performance metrics such as the dissolution behavior.

AUTHOR INFORMATION

Corresponding Author

*Tel.: (765) 494-8776 (M.T.H.); (765) 496-6614 (L.S.T.). Fax: (765) 494-0805 (M.T.H.); (765) 494-6545 (L.S.T.). E-mail: mtharris@purdue.edu (M.T.H.); lstaylor@purdue.edu (L.S.T.).

Notes

The authors declare no competing financial interest.

ACKNOWLEDGMENTS

Portions of this work were performed at the Advanced Photon Source (APS) Sector 12-ID-B, Argonne National Laboratory. Use of the APS was supported by the U.S. Department of Energy, Office of Science, and Office of Basic Energy Sciences. We acknowledge the National Science Foundation Engineering Research Center for Structured Organic Particulate Systems (EEC-0540855) for financial support. S.J.T. and G.J.S. gratefully acknowledge additional support from NIH-R01GM103401.

REFERENCES

- (1) Leuner, C.; Dressman, J. Improving Drug Solubility for Oral Delivery Using Solid Dispersions. *Eur. J. Pharm. Biopharm.* **2000**, *50*, 47–60.
- (2) Chiou, W. L. Pharmaceutical Applications of Solid Dispersion Systems: X-Ray Diffraction and Aqueous Solubility Studies on Griseofulvin-Polyethylene Glycol 6000 Systems. *J. Pharm. Sci.* **1977**, *66*, 989–991.
- (3) Serajuddin, A. T. M. Solid Dispersion of Poorly Water-Soluble Drugs: Early Promises, Subsequent Problems, and Recent Breakthroughs. *J. Pharm. Sci.* **1999**, *88*, 1058–1066.
- (4) Craig, D. Q. M. The Mechanisms of Drug Release from Solid Dispersions in Water-Soluble Polymers. *Int. J. Pharm.* **2002**, *231*, 131–144.
- (5) Matteucci, M. E.; Brettmann, B. K.; Rogers, T. L.; Elder, E. J.; Williams, R. O., 3rd.; Johnston, K. P. Design of Potent Amorphous Drug Nanoparticles for Rapid Generation of Highly Supersaturated Media. *Mol. Pharmaceutics* **2007**, *4*, 782–793.
- (6) Matteucci, M. E.; Miller, M. A.; Williams, R. O., III; Johnston, K. P. Highly Supersaturated Solutions of Amorphous Drugs Approaching Predictions from Configurational Thermodynamic Properties. *J. Phys. Chem. B* **2008**, *112*, 16675–16681.
- (7) Craig, D. Q. M. Polyethylene Glycols and Drug Release. *Drug Dev. Ind. Pharm.* **1990**, *16*, 2501–2526.
- (8) Mahlin, D.; Ridell, A.; Frenning, G.; Engström, S. Solid-State Characterization of PEG 4000/Monolein Mixtures. *Macromolecules* **2004**, *37*, 2665–2667.
- (9) Unga, J.; Matsson, P.; Mahlin, D. Understanding Polymer-Lipid Solid Dispersions—the Properties of Incorporated Lipids Govern the Crystallization Behavior of PEG. *Int. J. Pharm.* **2010**, *386*, 61–70.
- (10) Lloyd, G. R.; Craig, D. Q. M.; Smith, A. An Investigation into the Melting Behavior of Binary Mixes and Solid Dispersions of Paracetamol and PEG 4000. *J. Pharm. Sci.* **1997**, *86*, 991–996.
- (11) Lloyd, G. R.; Craig, D. Q. M.; Smith, A. An Investigation into the Production of Paracetamol Solid Dispersions in PEG 4000 Using Hot Stage Differential Interference Contrast Microscopy. *Int. J. Pharm.* **1997**, *158*, 39–46.
- (12) Lin, C. W.; Cham, T. M. Effect of Particle Size on the Available Surface Area of Nifedipine from Nifedipine-Polyethylene Glycol 6000 Solid Dispersions. *Int. J. Pharm.* **1996**, *127*, 261–272.
- (13) Ginés, J. M.; Arias, M. J.; Moyano, J. R.; Sánchez-Soto, P. J. Thermal Investigation of Crystallization of Polyethylene Glycols in Solid Dispersions Containing Oxazepam. *Int. J. Pharm.* **1996**, *143*, 247–253.
- (14) Zhu, Q.; Harris, M. T.; Taylor, L. S. Modification of Crystallization Behavior in Drug/Polyethylene Glycol Solid Dispersions. *Mol. Pharmaceutics* **2012**, *9*, 546–553.
- (15) Zhu, Q.; Taylor, L. S.; Harris, M. T. Evaluation of the Microstructure of Semicrystalline Solid Dispersions. *Mol. Pharmaceutics* **2010**, *7*, 1291–1300.
- (16) Zhu, Q.; Harris, M. T.; Taylor, L. S. Time-Resolved SAXS/WAXS Study of the Phase Behavior and Microstructural Evolution of Drug/PEG Solid Dispersions. *Mol. Pharmaceutics* **2011**, *8*, 932–939.
- (17) Wanapun, D.; Kestur, U. S.; Kissick, D. J.; Simpson, G. J.; Taylor, L. S. Selective Detection and Quantitation of Organic Molecule Crystallization by Second Harmonic Generation Microscopy. *Anal. Chem.* **2010**, *82*, 5425–5432.
- (18) Wampler, R. D.; Kissick, D. J.; Dehen, C. J.; Gualtieri, E. J.; Grey, J. L.; Wang, H. F.; Thomson, D. H.; Cheng, J. X.; Simpson, G. J. Selective Detection of Protein Crystals by Second Harmonic Microscopy. *J. Am. Chem. Soc.* **2008**, *130*, 14076–14077.
- (19) Simpson, G. J. Molecular Origins of the Remarkable Chiral Sensitivity of Second-Order Nonlinear Optics. *ChemPhysChem* **2004**, *5*, 1301–1310.
- (20) Flory, P. J. *Principles of Polymer Chemistry*; Cornell University Press: New York, 1953.
- (21) Nishi, T.; Wang, T. T. Melting Point Depression and Kinetic Effects of Cooling on Crystallization in Poly(Vinylidene Fluoride)-Poly(Methyl Methacrylate) Mixtures. *Macromolecules* **1975**, *8*, 909–915.
- (22) Hoei, Y.; Yamaura, K.; Matsuzawa, S. A Lattice Treatment of Crystalline Solvent-Amorphous Polymer Mixtures on Melting Point Depression. *J. Phys. Chem.* **1992**, *96*, 10584–10586.
- (23) Marsac, P. J.; Shamblin, S. L.; Taylor, L. S. Theoretical and Practical Approaches for Prediction of Drug-Polymer Miscibility and Solubility. *Pharm. Res.* **2006**, *23*, 2417–2426.
- (24) Rumondor, A. C. F.; Marsac, P. J.; Stanford, L. A.; Taylor, L. S. Phase Behavior of Poly(Vinylpyrrolidone) Containing Amorphous Solid Dispersions in the Presence of Moisture. *Mol. Pharmaceutics* **2009**, *6*, 1492–1505.
- (25) Buckley, C. P.; Kovacs, A. J. Melting Behavior of Low Molecular Weight Poly(Ethylene-Oxide) Fractions 2. Folded Chain Crystals. *Colloid Polym. Sci.* **1976**, *254*, 695–715.
- (26) Cheng, S. Z. D.; Zhang, A. Q.; Chen, J. H.; Heberer, D. P. Nonintegral and Integral Folding Crystal Growth in Low-Molecular Mass Poly(Ethylene Oxide) Fractions. I. Isothermal Lamellar Thickening and Thinning. *J. Polym. Sci., Part B: Polym. Phys.* **1991**, *29*, 287–297.
- (27) Balta Calleja, F. J.; Vonk, C. G. *X-ray Scattering of Synthetic Polymers*; Elsevier Science: New York, 1989.
- (28) Lisowski, M. S.; Liu, Q.; Cho, J.; Runt, J. Crystallization Behavior of Poly(Ethylene Oxide) and Its Blends Using Time-

Resolved Wide- and Small-Angle X-Ray Scattering. *Macromolecules* 2000, 33, 4842–4849.

(29) Kim, C. Y.; Kim, Y. C.; Kim, S. C. Temperature Dependence of the Nucleation Effect of Sorbitol Derivatives on Polypropylene Crystallization. *Polym. Eng. Sci.* 1993, 33, 1445–1451.